Liu *et al.*
Chinese Journal of Mechanical Engineering (2023) 36:96
https://doi.org/10.1186/s10033-023-00910-9

Chinese Journal of Mechanical Engineering

ORIGINAL ARTICLE

Open Access

Model of Surface Texture for Honed Gear Considering Motion Path and Geometrical Shape of Abrasive Particle

Yuhu Liu[1,2], Xiaohui Huang[1,2], Huajun Cao[1,2*], Jiacheng Wang[1,2] and Huapan Xiao[1,2]

Abstract

Gear power-honing is mainly applied to finish small and medium-sized automotive gears, especially in new energy vehicles. The distinctive curved surface texture greatly improves the noise emission and service life of honed gears. The surface texture for honed gear considering the motion path and geometrical shape of abrasive particles has not been investigated. In this paper, the kinematics of the gear honing process is analyzed, and the machining marks produced by the abrasive particles of honing wheel scratching abrasive particles against the workpiece gear are calculated. The tooth surface roughness is modeled considering abrasive particle shapes and material plastic pile-ups. This results in a mathematical model that characterizes the structure of the tooth surface and the orientation of the machining marks. Experiments were used to verify the model, with a maximum relative error of less than 10% when abrasive particles are spherical. Based on this model, the effects of process parameters on the speeds of discrete points on the tooth flank, orientations of machining marks and roughness are discussed. The results show that the shaft angle between the workpiece gear and the honing wheel and the speed of the honing wheel is the main process parameters affecting the surface texture. This research proposes a surface texture model for honed gear, which can provide a theoretical basis for optimizing process parameters for gear power-honing.

Keywords Hardened gear, Gear power-honing, Surface texture, Roughness

1 Introduction

Hardened gear is a key component of the transmission system of new energy vehicles (NEVs), which is one of the main noise sources of NEVs [1]. Finishing processes for hardened gears have received increased attention as NEVs place higher demands on reducing gear meshing noise [2]. Gear grinding and gear power honing are the two main methods for finishing hardened gears [3]. Compared with gear grinding, gear power honing can avoid tooth surface burn due to its low grinding speed [4]. On the other hand, power honing will produce a unique texture on the tooth surface, resulting in low noise performance [4–7]. This is one of the most important advantages of power honing. However, the mechanism for forming features such as texture distribution and roughness on power-honed tooth surfaces has not been adequately investigated in published sources. Therefore, this study aims to discuss the honed gear surface texture formation mechanism and propose a modeling method to provide a theoretical basis for optimizing process parameters.

Some scholars have conducted in-depth research on the processing mechanism, forming characteristics of gear honing and the optimization and modification of honed gear [8–13]. For example, Bergs [14] calculated the velocity at the contact point between the tool and

*Correspondence:
Huajun Cao
hjcao@cqu.edu.cn
[1] College of Mechanical and Vehicle Engineering, Chongqing University, Chongqing 400044, China
[2] State Key Laboratory of Mechanical Transmissions, Chongqing University, Chongqing 400044, China

the workpiece and proposed a gear-honing process force model to improve the robustness of the honing process. Liang et al. [15] established the vector expression of cutting speed at the contact point for gear external honing and introduced a relationship between cutting speed at contact points and the surface quality of gears. Furthermore, it confirmed that the surface texture of the honed gear has a visible difference from the top to the root of the tooth. Talu et al. [16] compared the tooth surface textures of straight bevel gears using pulsed electrochemical honing and pulsed electrochemical finishing processes to provide support for process parameter optimization. Yuan et al. [17] proposed a tooth surface roughness modeling method based on the conical abrasive grain assumption, established a roughness model along the tooth surface and tooth orientation direction, and investigated the effect of the axis intersection angle on the roughness. Han et al. [18] developed a roughness model based on experimental data using the response surface method and similarly discussed the effect of process parameters on roughness. The above models can reflect the complex motion and contact states in gear honing. However, there are some shortcomings in these models regarding surface textures. For example, the modeling process may ignore the influence of different abrasive shapes and the variation of the roughness distribution at different gradients of the tooth surface due to specific textures. Yang et al. [19] have mentioned that the irregular texture produced by power honing can reduce gear meshing noise. Therefore, it is necessary to study the surface texture by obtaining the machining marks on the honed gear first. Then the process parameters are guided to reduce the NVH of NEVs by using the surface texture characteristics of honing gears.

The gear-honing tool is essentially a grinding wheel in the shape of an internal helical gear [20]. The workpiece material is removed and the tooth flank is finished by rubbing, ploughing, and cutting abrasive particles. In the process, machining marks are generated. Ono et al. [21] built the classical theory of grinding mechanism based on the concept of subsequent grinding edge. Based on the assumption of uniformly distributed abrasive particles, Wang et al. [22] obtained the surface roughness of an aero-engine blade with different curvature variations by superimposing a simulation model of contact deformation at the grinding interface with the equations of the trajectory of the abrasive grains. Kang et al. [23] constructed a model of the distribution, size, and shape of active and broken abrasive grains based on image processing data and established a three-dimensional morphological model of the grinding wheel that agrees with the actual. Elwasli et al. [24] discussed the effect of initial surface topography on wear and friction behavior and accurately predicted the wear behavior of smooth and rough surfaces. Xiong et al. [25] studied the mechanism of cutting-edge burr formation by considering the material build-up effect in the micro drill grinding process. Moreover, much concrete research discussed the relationship between the surface roughness and the number of effective abrasive particles according to the mass of grinding test data [26, 27]. These researches establish many roughness models considering the abrasive particle shape, material plastic pile-up and effective abrasive particle number for ground surface topography/structure. However, research on gear has focused on optimizing grinding process parameters by investigating the mechanism of surface texture generation on ground teeth [8, 28]. The model of surface texture for honed gear considering these characteristics is still scarce. Therefore, it is important to study the honed surface texture by calculating its roughness considering the above characteristics.

The literature review shows that modeling the surface texture of honed gears suffers from a lack of consideration of different abrasive shapes and the distribution of different gradients of roughness on tooth surfaces. In conjunction with grinding theory, a theoretical model of the surface texture of honed gears is proposed in this study to address these gaps. The machining marks on the tooth flank were obtained by numerical calculation. The roughness was modeled considering the effects of abrasive particle geometrical shape and material plastic pile-up to quantify the honed surface texture. A series of experiments on gear power-honing were carried out to verify the effectiveness and robustness of the roughness model. Moreover, the speeds of discrete points on the tooth flank, the orientations of machining marks and the roughness of honed gear were discussed under different processing parameters.

2 Theoretical Model

The common application of gear power-honing is the hard finishing of external gears. In this case, the contact between a workpiece and a honing tool with geometrically undefined cutting edges is equivalent to the contact of a gear pair with intersecting axes. In the modeling, a series of machining marks are obtained by numerical calculation, generated by scratching of abrasive particles, and superimposed to build the surface texture of honed gear.

2.1 Kinematics of Gear Honing Process

The relationship between workpiece angular velocity $\boldsymbol{\omega}_{\mathrm{w}}$ and honing tool angular velocity $\boldsymbol{\omega}_{\mathrm{h}}$ is expressed as:

$$\frac{|\boldsymbol{\omega}_{\mathrm{w}}|}{|\boldsymbol{\omega}_{h}|}=\frac{\varphi_{\mathrm{w}}(t)}{\varphi_{\mathrm{h}}(t)}=\frac{n_{\mathrm{h}}}{n_{\mathrm{w}}}=i, \quad (t \geq 0), \tag{1}$$

where $\phi_{\mathrm{w}}(t)$ and $\phi_{\mathrm{h}}(t)$ are rotation angles of workpiece and honing tool, which are equal to the dot product of

workpiece angular velocity $\boldsymbol{\omega}_w$ and honing tool angular velocity $\boldsymbol{\omega}_h$ over time, respectively; n_w and n_h are the tooth number of workpiece and honing tool, respectively; i is a transmission ratio.

As shown in Figure 1, spatial coordinate systems of workpiece and honing tool are established, including a workpiece fixed coordinate system S_{wf} (O_{wf}-x_{wf}-y_{wf}-z_{wf}), a honing tool fixed coordinate system S_{hf} (O_{hf}-x_{hf}-y_{hf}-z_{hf}), a workpiece rotation coordinate system S_w (O_w-x_w-y_w-z_w) and a honing tool rotation coordinate system S_h (O_h-x_h-y_h-z_h). The origins of coordinate systems S_{wf} and S_w are located at the centroid of workpiece. The origins of coordinate system S_{hf} and S_h are fixed at the centroid of honing tool. Any two axes in a coordinate system are perpendicular to each other. The axes x_{wf}, x_w, x_{hf}, and x_h coincide and pass through the centroids of the workpiece and honing wheel. The axes z_w and z_h are perpendicular to the end faces of workpiece and honing tool, respectively. d is the distance between the workpiece centroid and honing tool centroid. γ is a cross axis angle which is equal to the difference between helix angle of honing tool (β_h) and helix angle of workpiece (β_w), i.e., $\gamma = |\beta_h - \beta_w|$.

In coordinate system S_w, the tooth flank of workpiece is an involute helicoid. The tooth flank equation $\boldsymbol{r}_w(\zeta, \eta)$ of workpiece is [29]:

$$\boldsymbol{r}_w(\zeta,\eta) = \begin{bmatrix} x_w \\ y_w \\ z_w \end{bmatrix} = \begin{bmatrix} r_b\cos(\eta+\zeta) + r_b\zeta\sin(\eta+\zeta) \\ r_b\sin(\eta+\zeta) - r_b\zeta cos(\eta+\zeta) \\ \eta p_w \end{bmatrix}, \tag{2}$$

where r_b is the basic circle radius of workpiece; η is an angle parameter of the intersection point between involute and base circle, which varies from η_s to η_f; ζ is an angle parameter of involute, which varies from ζ_s to ζ_f; p_w is the workpiece lead.

The relative velocity $\boldsymbol{v}$ between workpiece and honing tool can be calculated by:

$$\begin{aligned} \boldsymbol{v} &= \boldsymbol{v}_{wf,w} - \boldsymbol{v}_{wf,h} \\ &= \boldsymbol{\omega}_{wf,w} \times \boldsymbol{r}_{wf,w}(\zeta,\eta,\varphi_w(t)) - \boldsymbol{\omega}_{wf,h} \times \boldsymbol{r}_{wf,h}(\zeta,\eta,\varphi_w(t)) \\ &= \omega_w \begin{bmatrix} -y_w(1-\cos\gamma/i) + z_w\cos\varphi_w(t)\cdot\sin\gamma/i \\ -d\sin\varphi_w(t)\cdot\cos\gamma/i \\ x_w(1-\cos\gamma/i) - z_w\sin\varphi_w(t)\cdot\sin\gamma/i \\ -d\cos\varphi_w(t)\cdot\cos\gamma/i \\ -(x_w\cos\varphi_w(t) - y_w\sin\varphi_w(t) + d)\cdot\sin\gamma/i \end{bmatrix}, \end{aligned} \tag{3}$$

where $\boldsymbol{v}_{wf,w}$ and $\boldsymbol{v}_{wf,h}$ are velocities on the tooth flank of workpiece and honing tool, respectively; $\boldsymbol{\omega}_{wf,w}$ and $\boldsymbol{\omega}_{wf,h}$ are angular velocities of workpiece and honing tool, respectively; $\boldsymbol{r}_{wf,w}(\zeta, \eta, \phi_w(t))$ and $\boldsymbol{r}_{wf,h}(\zeta, \eta, \phi_w(t))$ are the tooth flank equations of workpiece and honing tool in coordinate system S_{wf}, respectively.

According to the meshing theory, the meshing equation is expressed as follows:

$$\boldsymbol{v}(\zeta_1,\eta_1,\varphi_w(t))\cdot\boldsymbol{n} = 0, \tag{4}$$

where the normal vector $\boldsymbol{n}$ of workpiece tooth flank in coordinate system S_{wf} is obtained by Eq. (5):

$$\begin{aligned} \boldsymbol{n} &= \begin{bmatrix} n_x & n_y & n_z \end{bmatrix}^T \\ &= \begin{bmatrix} \zeta\cdot r_b\cdot p_w\cdot\sin(\eta+\zeta+\varphi_w(t)) \\ -\zeta\cdot r_b\cdot p_w\cdot\cos(\eta+\zeta+\varphi_w(t)) \\ \zeta\cdot r_b^2 \end{bmatrix}, \end{aligned} \tag{5}$$

where n_x, n_y, and n_z are the components of normal vector $\boldsymbol{n}$ along x_{wf}, y_{wf}, and z_{wf} coordinate axes, respectively.

Substituting Eqs. (3) and (5) into Eq. (4), the meshing equation can be changed as:

$$U\cos\varphi_w(t) - V\sin\varphi_w(t) = W, \tag{6}$$

where U, V, and W are expressed as:

$$\begin{cases} U = -(n_{w,z}\cdot x_w - n_{w,x}\cdot z_w)\cdot\sin\gamma - n_{w,y}\cdot d\cdot\cos\gamma, \\ V = -(n_{w,z}\cdot y_w - n_{w,y}\cdot z_w)\cdot\sin\gamma + n_{w,x}\cdot d\cdot\cos\gamma, \\ W = (\cos\gamma - 1/i)\cdot(n_{w,y}\cdot x_w - n_{w,x}\cdot y_w) + n_{w,z}\cdot d\cdot\sin\gamma. \end{cases} \tag{7}$$

The honing tool tooth profile equation is obtained, as shown in Eq. (8)

$$\begin{cases} \boldsymbol{r}_w = \boldsymbol{r}_w(\zeta,\eta), \\ \boldsymbol{r}_h = \boldsymbol{M}_{h,w}\boldsymbol{r}_w, \\ U\cos\varphi_w(t) - V\sin\varphi_w(t) = W, \end{cases} \tag{8}$$

where $\boldsymbol{M}_{h,w}$ is the transformation matrice for coordinate systems S_w-S_h.

During analyzing the contact between workpiece and honing tool, the tooth flank of honing tool is enveloped by the tooth flank of workpiece based on the envelope theory. In gear power-honing, the tooth flank of workpiece is enveloped by the tooth flank of honing tool. To ensure that the tooth flank of honed gear is an involute helicoid, the contact lines produced by above two enveloping processes should be consistent. Consequently, the coordinates of all points on the tooth flank of workpiece need to satisfy Eq. (9).

$$U^2 + V^2 \geq W^2. \tag{9}$$

The derivation of Eq. (9) is shown in Eqs. (10)–(16). Firstly, Eq. (6) can be changed as:

$$\cos(\delta + \varphi_w(t)) = \frac{W}{\sqrt{U^2+V^2}}, \tag{10}$$

where $\delta = \arctan(V/U)$. Eq. (10) has a real solution only when $-1 \leq \cos(\delta+\phi_w(t)) \leq 1$, i.e., $U^2+V^2 \geq W^2$. Those points on conjugate surfaces corresponding to all real

solution form the effective region. Those points satisfying $U^2+V^2=W^2$ construct the meshing boundary line.

Secondly, Eq. (6) can be also written as:

$$f(\zeta,\eta,\varphi_{\mathrm{w}}(t))=U\cos\varphi_{\mathrm{w}}(t)-V\sin\varphi_{\mathrm{w}}(t)-W=0. \tag{11}$$

Thirdly, by deriving Eq. (9) from ϕ_{w}, it can be obtained as:

$$\frac{\partial f}{\partial\varphi_{\mathrm{w}}(t)}(\zeta,\eta,\varphi_{\mathrm{w}}(t))=-U\sin\varphi_{\mathrm{w}}(t)-V\cos\varphi_{\mathrm{w}}(t). \tag{12}$$

By squaring Eqs. (6) and (9), it has

$$\begin{cases} U^2\cos^2\varphi_{\mathrm{w}}(t)+V^2\sin^2\varphi_{\mathrm{w}}(t) \\ -2UV\sin\varphi_{\mathrm{w}}(t)\cos\varphi_{\mathrm{w}}(t)=W^2, \\ U^2\sin^2\varphi_{\mathrm{w}}(t)+V^2\cos^2\varphi_{\mathrm{w}}(t) \\ +2UV\sin\varphi_{\mathrm{w}}(t)\cos\varphi_{\mathrm{w}}(t)=(\partial f/\partial\varphi_{\mathrm{w}}(t))^2. \end{cases} \tag{13}$$

Finally, it can be obtained as:

$$U^2+V^2=W^2+(\partial f/\partial\varphi_{\mathrm{w}}(t))^2. \tag{14}$$

On the meshing boundary line, $U^2+V^2=W^2$, then

$$\frac{\partial f}{\partial\varphi_{\mathrm{w}}(t)}(\zeta,\eta,\varphi_{\mathrm{w}}(t))=0. \tag{15}$$

Because $\partial f/\partial\phi_{\mathrm{w}}=0$ is derived from the conjugate meshing equation $f=0$, those points on the workpiece tooth flank satisfying $\partial f/\partial\phi_{\mathrm{w}}=0$ and $f=0$ form the meshing boundary line.

$$\begin{cases} \boldsymbol{r}_{\mathrm{wf,w}}=\boldsymbol{r}_{\mathrm{wf,w}}(\zeta,\eta,\varphi_{\mathrm{w}}(t)), \\ f(\zeta,\eta,\varphi_{\mathrm{w}}(t))=0, \\ \partial f(\zeta,\eta,\varphi_{\mathrm{w}}(t))/\partial\varphi_{\mathrm{w}}(t)=0. \end{cases} \tag{16}$$

2.2 Surface Modeling of Honed Gear

The distinctive structure of honed gear surface contains numerous curved machining marks which result from the scratching of abrasive particles with the rotation of honing tool and workpiece.

In the process of gear power-honing, any micro-area of the tooth surface is engaged in time sequence, and the dynamic meshing contact point is marked as B_e, and its position vector expression ($\boldsymbol{B}_e$) must meet the requirements of Eq. (17).

$$\begin{cases} \boldsymbol{B}_e(T)-\boldsymbol{r}_{\mathrm{w}}(\zeta_{e1},\eta_{e2})=0 \quad (e=1,2,\ldots,k;\ e1\le m;\ e2\le n), \\ U(\zeta_{e1},\eta_{e2})\cdot\cos\varphi_{\mathrm{w}}(T)-V(\zeta_{e1},\eta_{e2})\cdot\sin\varphi_{\mathrm{w}}(T)-W(\zeta_{e1},\eta_{e2})=0. \end{cases} \tag{17}$$

When one of ζ_{e1} or η_{e2} is fixed, another is solved by carrying out numerical iterative search algorithms like Newton-Raphson method.

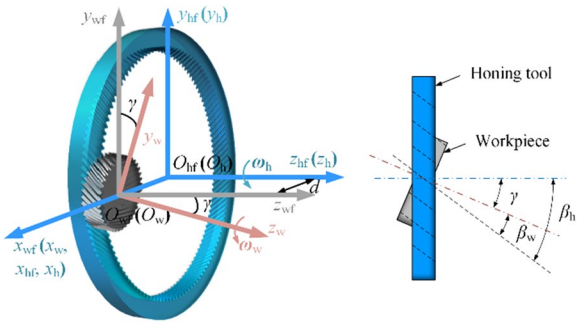

Figure 1 Spatial coordinate systems of workpiece and honing tool and schematic of the contact between workpiece and honing tool

In this section, the dynamic meshing contact point B_e is assumed to be the center of the cross section where an abrasive particle of honing tool penetrates workpiece. By the numerical calculation for motion paths of abrasive particles, machining marks are obtained. The surface model of honed gear is established in coordinate system S_{wf} for honed gear as following procedures (Table 1).

Step 1: A point B_e is obtained under a certain rotation angle $\phi_{\mathrm{h}}(T)$, as shown in Figure 2a. The point $B_e^{(0)}$ ($e=1,2,\ldots,k$) is taken as an endpoint of each machining mark Γ. The generation process of the eth ($1\le e\le k$) machining mark Γ_e is taken as an example.

Step 2: By rotating the honing tool with a small discrete rotation angle $\Delta\phi_{\mathrm{h},e}$, point $B_e^{(0)}$ moves to point $B_e^{(1)}$ with relative velocity $\boldsymbol{v}_e^{(0)}$, as shown in Figure 2b. The radius vector $\boldsymbol{B}_e^{(1)}$ of point $B_e^{(1)}$ is judged whether it meets Eqs. (6) and (9) simultaneously. If it meets, the equation $\boldsymbol{\Gamma}_e^{(1)}$ of machining mark $\Gamma_e^{(1)}$ between two points $B_e^{(0)}$ and $B_e^{(1)}$ is obtained; if it does not, the calculation stops. The radius vector $\boldsymbol{B}_e^{(1)}$ is expressed as:

$$\boldsymbol{B}_e^{(1)}=\boldsymbol{B}_e^{(0)}+\Delta\varphi_{\mathrm{h},e}\cdot\boldsymbol{v}_e^{(0)}, \tag{18}$$

where $\boldsymbol{v}_e^{(0)}$ satisfies to the Eq (3).

The equation $\boldsymbol{\Gamma}_e^{(1)}$ of machining mark $\Gamma_e^{(1)}$ is obtained by:

$$\boldsymbol{\Gamma}_e^{(1)}=\boldsymbol{B}_e^{(1)}-\boldsymbol{B}_e^{(0)}. \tag{19}$$

Step 3: By continuously rotating the honing tool with m small discrete rotation angles $\Delta\phi_{\mathrm{h},e}$, point $B_e^{(1)}$ eventually moves to point $B_e^{(m)}$, as shown in Figure 2c. It is assumed that radius vector $\boldsymbol{B}_e^{(m+1)}$ of point $B_e^{(m+1)}$ does not meet Eq. (6) or Eq. (9). The radius vector $\boldsymbol{B}_e^{(j)}$ of

Table 1 Surface modelling process for honed gears

for $e \le k$,
when $t = T$, get $\boldsymbol{B}_e$ by Eq. (10)
if $\Delta\varphi_{h,e} \neq 0$, get $\boldsymbol{B}_e^{(1)}$ by Eq. (11)
if $\boldsymbol{B}_e^{(1)}$ meets Eqs. (6) and (9), get $\boldsymbol{\Gamma}_e^{(1)}$
for $j \le m + 1$,
get $\boldsymbol{B}_e^{(j)}$, and $\boldsymbol{\Gamma}_e^{(j)}$
j =+ 1
until $\boldsymbol{B}_e^{(m+1)}$ does not meets Eqs. (6) and (9)
get $\boldsymbol{\Gamma}_e$
e =+ 1
get S_h

point $B_e^{(j)}$, and the equation $\boldsymbol{\Gamma}_e^{(j)}$ of machining mark $\Gamma_e^{(j)}$ between two points $B_e^{(j-1)}$ and $B_e^{(j)}$ (j=1, 2, 3, ..., m) are respectively expressed as:

$$\begin{aligned}\boldsymbol{B}_e^{(j)} &= \boldsymbol{B}_e^{(j-1)} + \Delta\varphi_{h,e} \cdot \boldsymbol{v}_e^{(j-1)} \\ &= \boldsymbol{B}_e^{(0)} + \Delta\varphi_{h,e} \cdot \boldsymbol{v}_e^{(0)} + \Delta\varphi_{h,e} \cdot \boldsymbol{v}_e^{(1)} + \ldots + \Delta\varphi_{h,e} \cdot \boldsymbol{v}_e^{(j-1)} \\ &= \boldsymbol{B}_e^{(0)} + \Delta\varphi_{w,e}/i \cdot \boldsymbol{v}_e^{(0)} + \Delta\varphi_{w,e}/i \cdot \boldsymbol{v}_e^{(1)} + \ldots + \Delta\varphi_{w,e}/i \cdot \boldsymbol{v}_e^{(j-1)},\end{aligned} \tag{20}$$

$$\begin{aligned}\boldsymbol{\Gamma}_e^{(j)} &= \boldsymbol{B}_e^{(j)} - \boldsymbol{B}_e^{(j-1)} = \Delta\varphi_{h,e} \cdot \boldsymbol{v}_e^{(j-1)} \\ &= \Delta\varphi_{w,e} \cdot \boldsymbol{v}_e^{(j-1)}/i,\end{aligned} \tag{21}$$

where $\boldsymbol{v}_e^{(j-1)}$ is the relative velocity at point $B_e^{(j-1)}$.

Step 4: As shown in Figure 2d, the equation $\boldsymbol{\Gamma}_e$ of eth machining mark Γ_e is expressed as:

$$\boldsymbol{\Gamma}_e = \left\{ \boldsymbol{\Gamma}_e^{(0)}, \boldsymbol{\Gamma}_e^{(1)}, \boldsymbol{\Gamma}_e^{(2)}, \ldots, \boldsymbol{\Gamma}_e^{(m)} \right\}. \tag{22}$$

Step 5: All machining marks Γ_1, Γ_2, ..., Γ_k are calculated one by one, which constitute a complete honed tooth flank (S_h) with a distinctive structure. The S_h can be expressed as:

$$S_h = \{\boldsymbol{\Gamma}_1, \boldsymbol{\Gamma}_2, \boldsymbol{\Gamma}_3, \ldots, \boldsymbol{\Gamma}_e, \ldots, \boldsymbol{\Gamma}_k\}. \tag{23}$$

The machining marks produced by gear power-honing are some three-dimensional space curves. In this paper, the orientation of machining mark is characterized through angle between machining mark direction and tooth profile direction, as shown in Figure 2d, which is expressed as:

$$\lambda = \arccos\left(\frac{(\boldsymbol{B}_e^{(j)} - \boldsymbol{B}_e^{(j-1)}) \cdot \frac{\partial \boldsymbol{r}_w(\boldsymbol{B}_e^{(j)})}{\partial \zeta}}{\left|\boldsymbol{B}_e^{(j)} - \boldsymbol{B}_e^{(j-1)}\right| \cdot \left|\frac{\partial \boldsymbol{r}_w(\boldsymbol{B}_e^{(j)})}{\partial \zeta}\right|} \right) \cdot \frac{180^\circ}{\pi}. \tag{24}$$

If the calculated angle λ is larger than 90° by Eq. (24), angle λ is calculated by Eq. (25):

$$\lambda = 180^\circ - \arccos\left(\frac{(\boldsymbol{B}_e^{(j)} - \boldsymbol{B}_e^{(j-1)}) \cdot \frac{\partial \boldsymbol{r}_w(\boldsymbol{B}_e^{(j)})}{\partial \zeta}}{\left|\boldsymbol{B}_e^{(j)} - \boldsymbol{B}_e^{(j-1)}\right| \cdot \left|\frac{\partial \boldsymbol{r}_w(\boldsymbol{B}_e^{(j)})}{\partial \zeta}\right|} \right) \cdot \frac{180^\circ}{\pi}. \tag{25}$$

2.3 Roughness Modeling Considering Shape of Abrasive Particle

The material removal mechanism of cylindrical gear power-honing is similar to that of cylindrical grinding. The abrasive particles move along the machining marks and remove gear material, forming a series of micro-grooves. Roughness R_a is selected as a quantitative index to evaluate the distinctive surface texture. In

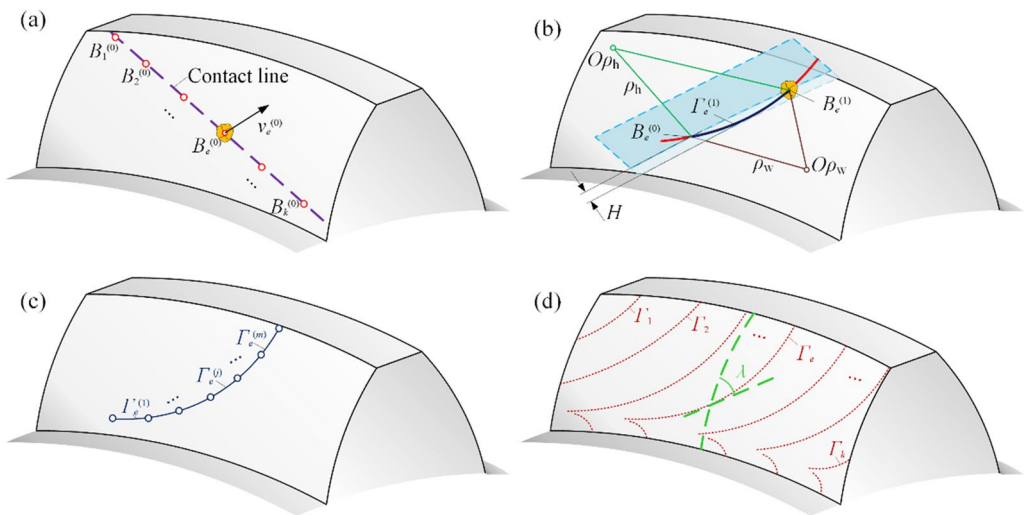

Figure 2 Modeling process of surface texture of honed gear

this section, a roughness model is developed considering the effects of abrasive particle geometrical shape and material plastic pile-up. The following assumptions are made firstly:

(1) Ignore an effect of vibration from gear honing machine;
(2) ignore the influence of thermal deformation on gear honing machine;
(3) and the abrasive particles are distributed uniformly on honing tool surface.

Based on the above assumptions, Ono et al. [21] proposed that the maximum groove height H caused by the scratching of abrasive particles on ground surface:

$$H = \left(\frac{15}{16} \cdot \Delta^3 \cdot \cot\theta \cdot p\right)^q, \tag{26}$$

where Δ is an average spacing between adjacent abrasive particles; θ is a half apex angle of the abrasive particle; p is a parameter determined by grinding conditions; q is a parameter related to the shape and distribution of abrasive particles (q=0.4 and 0.5 for conical and spherical abrasive particles, respectively).

However, the gear power-honing has more complex contact between workpiece and tool, and lower cutting speed, which differs from cylindrical grinding process. The complex contact mainly affects the orientation of machining marks. The equivalent curvature radius of workpiece is different from the directions on a tooth flank. Therefore, the influence of machining mark orientation and cutting speed needs to be taken into account in the calculation of parameter p, which can be expressed as:

$$p = \frac{1}{c} \cdot \frac{v_{w,\Gamma}}{v_{w,\Gamma} - v_{h,\Gamma}} \sqrt{\frac{1}{2}\left(\frac{1}{\rho_w} - \frac{1}{\rho_h}\right)}, \tag{27}$$

where c is the grinding times during a period of spark-out honing, which is related to honing tool speed and spark-out time; ρ_w and ρ_h are the curvature radii of workpiece and honing tool at a discrete point of the contact line, respectively, which are related with the corresponding normal curvatures κ_w and κ_h along the orientation of machining mark:

$$\kappa_w = 1/\rho_w, \tag{28}$$

$$\kappa_h = 1/\rho_h. \tag{29}$$

Considering the width of geometric contact between workpiece and honing tool, the normal curvatures κ_w and κ_h are replaced by average curvatures $\kappa_{w,\Gamma}$ and $\kappa_{h,\Gamma}$.

The speed $v_{w,\Gamma}$ of workpiece along the direction of machining mark is calculated by:

$$v_{w,\Gamma} = \boldsymbol{v}_{wf,w} \cdot \boldsymbol{\nu} \cdot \frac{1}{\|\boldsymbol{\nu}\|}. \tag{30}$$

The speed $v_{h,\Gamma}$ of honing tool along the direction of machining mark is calculated by:

$$v_{h,\Gamma} = \boldsymbol{v}_{wf,h} \cdot \boldsymbol{\nu} \cdot \frac{1}{\|\boldsymbol{\nu}\|}. \tag{31}$$

The material plastic pile-up is an inevitable phenomenon in abrasive machining. The degree of material pile-up is closely related to the hardness of honing tool and the shape/size of abrasive particles. For different shaped abrasive particles, the average spacing Δ of abrasive particles is [30, 31]

$$\Delta = \begin{cases} 65.3 M_{od}^{-1.4} \sqrt[3]{\dfrac{\pi}{32 - S_{tr} \cdot \frac{1}{N_e}}} & \text{for conical abrasive particle,} \\ 137.9 M_{od}^{-1.4} \sqrt[3]{\dfrac{\pi}{32 - S_{tr} \cdot \frac{1}{N_e}}} & \text{for spherical abrasive particle,} \end{cases} \tag{32}$$

where M_{od} is a granularity of abrasive particles; S_{tr} is an organization number; N_e is a coefficient on the number of effective abrasive particles [8]. By substituting Eq. (32) into Eq. (26), the maximum groove heights H_c and H_s corresponding to conical and spherical abrasive particles can be obtained.

Figure 3a and b shows the schematics of cross section of grooves caused by scratching of a conical abrasive and spherical abrasive, respectively. The height of material pile-up ridges h_c and h_s corresponding to conical and spherical abrasive particles is calculated by Eq. (33).

$$\begin{cases} h_c = \sqrt{\frac{1-\tau}{2}} H_c & \text{for conical abrasive particle,} \\ h_s = \frac{\sqrt{1-\tau}}{2} H_s & \text{for spherical abrasive particle,} \end{cases} \tag{33}$$

where τ is the material removal rate as shown in Eq. (34) [32].

$$\tau = \frac{A - (A_1 + A_2)}{A}, \tag{34}$$

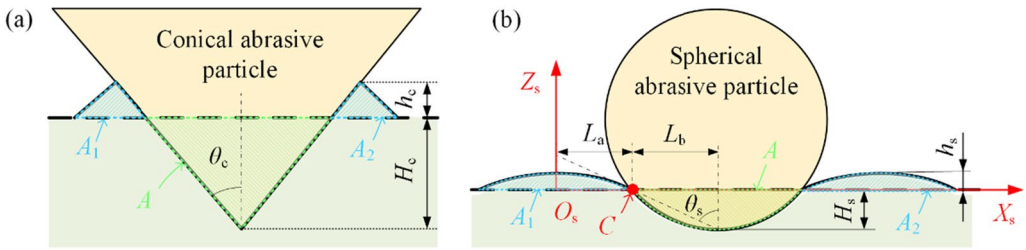

Figure 3 Cross section of scratch grooves including material pile-up ridges caused by scratching of **a** conical abrasive particle and **b** spherical abrasive particle. The cross section is vertical to movement direction of abrasive particle

where the A, A_1 and A_2 are shown in Figure 3 and can be obtained from basic geometric operations.

Therefore, considering the material plastic pile-up, the maximum groove height H becomes

$$H = \begin{cases} H_c + h_c & \text{for conical abrasive particle,} \\ H_s + h_s & \text{for spherical abrasive particle.} \end{cases} \tag{35}$$

Based on the relationship between the maximum groove height H and average roughness R_a [21], the surface roughness R_a can be established by:

$$R_a = 0.256H. \tag{36}$$

According to the theoretical model, if workpiece parameters, honing tool parameters, and honing process parameters are known, the surface texture of honed gear will be calculated and the distribution of roughness R_a will be obtained for honed gear.

3 Experimental Design

To validate the theoretical model, a series of honed gears were prepared under different process parameters which were selected from an effective range of gear-honing machines [17]. When the tooth number of honing tool is set to the maximum value of 113, the value of the rotation speed of honing tool, 876.11 r/min, is approximately at the midpoint of effective parameter range (720–1000 r/min); when the tooth number of honing tool is set to the minimum value of 105, the value of the rotation speed of honing tool, 900.95 r/min, is approximately at the golden section point of effective parameter range. The gears were first machined by a gear grinding machine (YW7232 CNC, CHMTI) under the same process parameters. The gear material was 20CrMnTiH. Next, the gears were finished by a gear honing machine (HMX-400, Fassler), as shown in Figure 4a. The parameters of workpiece and honing tool were shown in Table 2. The binder material of honing tool was ceramic, and the material of abrasive particles was microcrystalline corundum, as shown in Figure 4b. The infeed rate of honing tool, oscillation time and spark-out time are 0.408 mm/min, 45 s and 3.6 s, respectively.

The tooth flank structure and its roughness were measured. As shown in Figure 4c, the honed gears were cut by a diamond wire cutting machine to obtain many single teeth. The single teeth were cleaned by an ultrasonic cleaning machine with alcohol for at least 10 min. Seven small areas were selected from each tooth flank along the tooth longitudinal and tooth profile directions. The surface texture for every single tooth was obtained by an ultra-depth 3D microscope (VHX-1000C, Keyence). The local surface texture and roughness for each area were obtained by laser scanning confocal microscope (OLS4000, Olympus Corporation).

4 Results and Discussions

4.1 Experimental Results and Model Verification

Figure 5a and b shows the surface texture of honed gear and local surface textures of seven small areas selected from one of single teeth. From the surface texture, it has many curved machining marks like a fish skeleton. These machining marks asymptotically approach the pitch line and form a distinctive surface texture. The surface texture allows a nice adhesion of thin oil layer on a whole tooth flank, resulting in a low noise behavior of honed gears [6]. Due to the low cutting speed which usually varies from 0.5 m/s to 15 m/s in gear power-honing, thermal structural damages do not occur for honed gears. Three lines approximately vertical to the orientation of machining marks are selected randomly in each small area. By averaging the roughness R_a measured from the position of three lines for each area, the roughness R_a for each area is obtained, as shown in Table 3. According to the workpiece parameters, honing tool parameters, and process parameters, the roughness R_a is calculated by the proposed model, also shown in Table 3. The maximum relative error between the measured and calculated values of R_a is less than 10% when the shape of abrasive particle is assumed to be spherical. On the contrary, the maximum relative error is close to 40% when the shape of abrasive

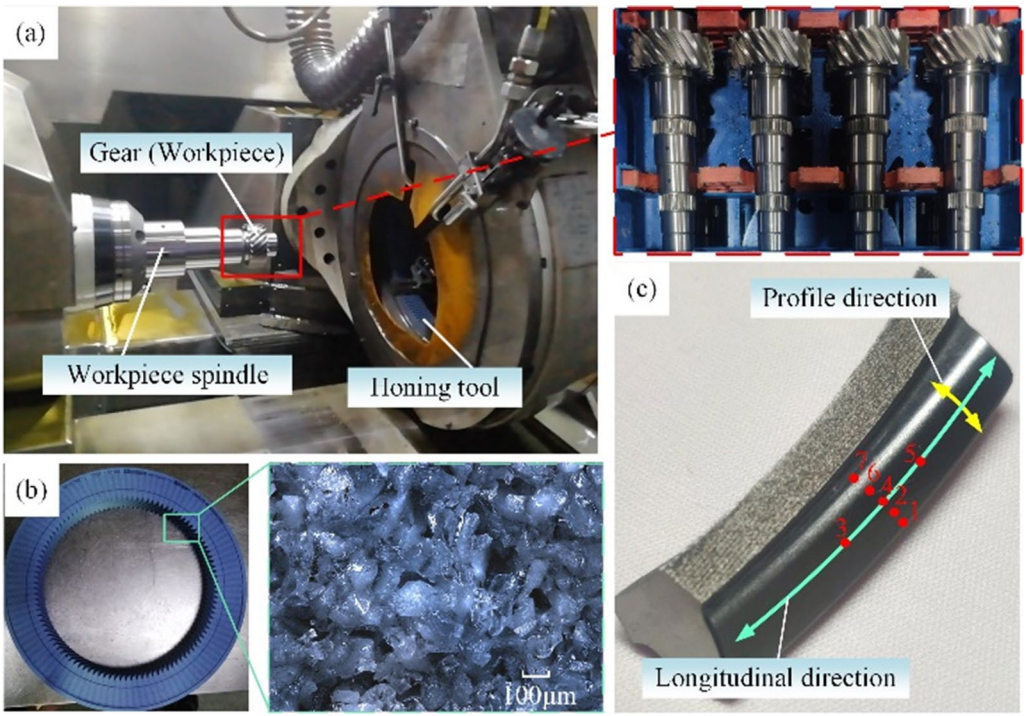

Figure 4 Experimental design for honing tests: **a** Gear honing machine and honed gears, **b** Honing tool and its surface abrasive particles, **c** Single tooth and its measurement areas

Table 2 Workpiece and honing tool parameters

Parameters	Workpiece	Honing tool
Tooth number	22	105/113
Module (mm)	2.627	2.627
Pressure angle (°)	20.222	20.222
Tooth width (mm)	31.2	34
Helix angle (°)	34	25.994/28.182
Modification coefficient (mm)	0.686	-
Granularity of abrasive particles	-	120 #
Organization number	-	4

particle is assumed to be conical. This indicates that the abrasive shape has a great influence on roughness and the spherical abrasive particle has more excellent prediction accuracy. The roughness results for the second and third groups (No. 2 and No. 3 in Table 3) show that roughness R_a increases as the speed of honing tool decreases. By comparing the roughness results for the first and second groups (No. 1 and No. 2 in Table 3), it shows that roughness R_a for the second group does not increase basically when the speed of honing tool decreases, which may be attributed to the decrease of tooth number and helix angle of honing tool.

The model is verified by experimental results, and applied to investigate the effects of process parameters on the distribution of speeds on tooth flank, orientations of machining marks, and roughness theoretically. The process parameters include cross axis angle γ, tooth number of honing tool n_h, and rotational speed of honing tool u_h. The speeds include $v_{wf,w}$, $v_{wf,h}$ and v. The values of $v_{wf,w}$, $v_{wf,h}$, v, angle λ, and roughness R_a are calculated under different process parameters (Table 4). Then, the distribution characteristics of the orientations of machining marks and roughness are discussed, which are introduced in detail in the following sections.

4.2 Effects of Process Parameters on Speed

Figure 6a, c and e shows three contour maps for speeds $v_{wf,w}$, $v_{wf,h}$ and v calculated under $\gamma=5°$, $n_h=113$, and $u_h=860$ r/min, respectively. It has been found that the X values of $v_{wf,w}$ and $v_{wf,h}$ increase linearly, while the value of v first decreases and then increases gradually from tooth root to tooth top at a fixed X value. Meanwhile, the values of $v_{wf,w}$, $v_{wf,h}$, and v always remain unchanged from the left end to the right end at a fixed Y value. This is because the values of $v_{wf,w}$ and $v_{wf,h}$ are proportional to the rotation radius of each contact point. According to the meshing theory of gear, the minimum value of relative speed v is located at pitch line of honed gear and

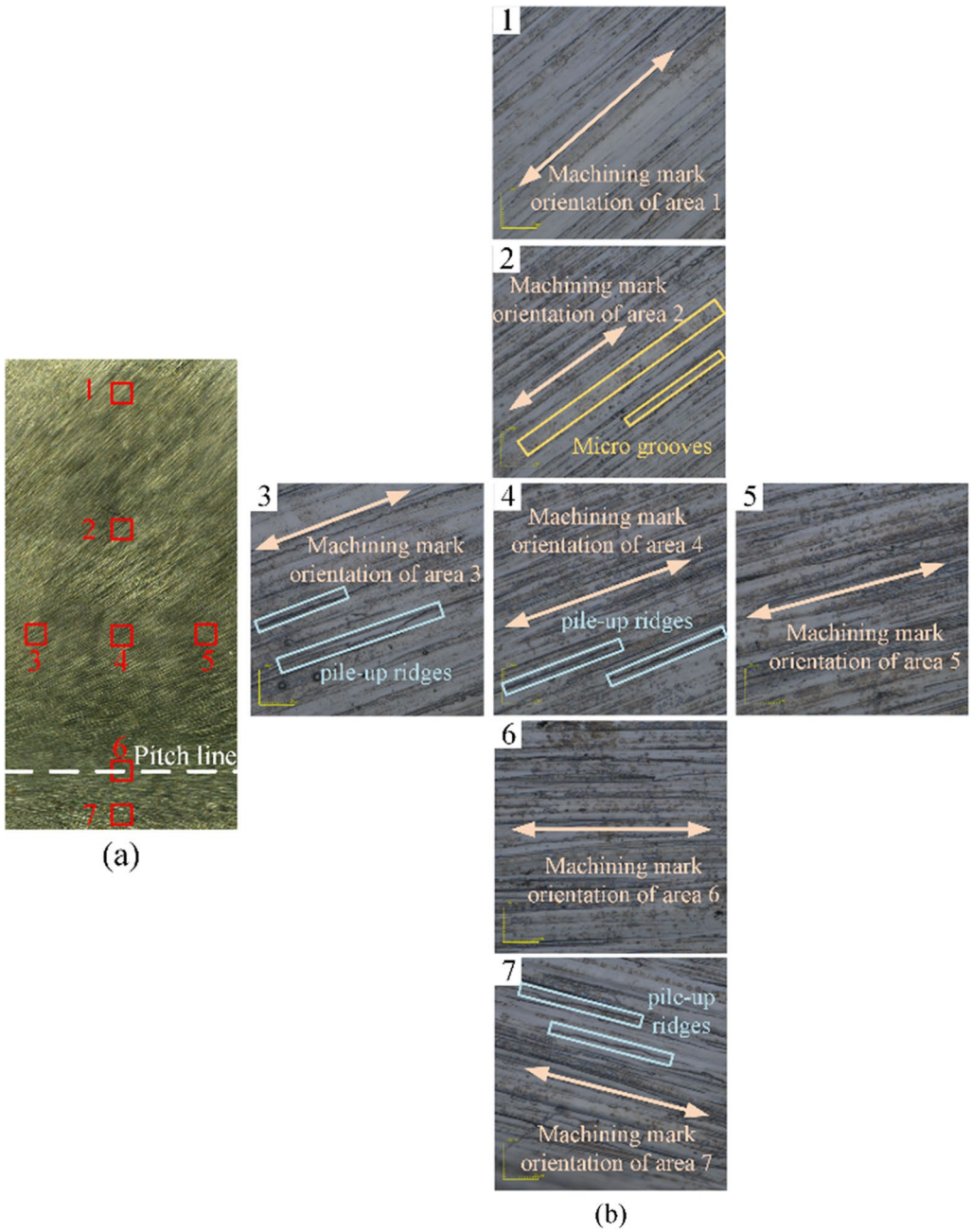

Figure 5 Measurement results of **a** complete surface texture obtained by an ultra-depth 3D microscope, **b** local surface textures of seven measured areas obtained by a laser scanning confocal microscope

increases gradually toward both sides of pitch line. Figure 6b, d and f shows the calculated values of $v_{wf,w}$, $v_{wf,h}$, and v at $X = 0$ mm under different process parameters (Table 4). It can be observed from Figure 6b that the values of $v_{wf,w}$ do not change with cross axis angle γ, while it increases with tooth number n_h or rotational speed u_h of honing tool. This is because when workpiece parameters are determined, the change of cross axis angle γ is only caused by the change of helix angle of honing tool, which will not affect workpiece speed. Moreover, according to Eq. (1), the change of the value of $v_{wf,w}$ with tooth number n_h and rotational speed u_h can be explained effectively. In Figure 6d, the value of $v_{wf,h}$ is negatively correlated with angle γ, while positively correlated with tooth number n_h and rotational speed u_h. The change of the values of $v_{wf,h}$ with angle γ can be explained by Eqs. (2) and (3).

Table 3 Process parameters for theoretical investigation

No.	Workpiece speed (r/min)	Tool speed (r/min)	Tool tooth number	Tool helix angle (°)	No. of measured area	Measured roughness R_a (μm)	Calculated R_a (μm)		Relative error (%)	
							Spherical abrasive particle	Conical abrasive particle	Spherical abrasive particle	Conical abrasive particle
1	4500	876.11	113	28.182	1	0.228	0.233	0.313	2.19	37.28
					2	0.336	0.340	0.417	1.19	24.11
					3	0.419	0.407	0.488	−2.86	16.47
					4	0.382	0.416	0.497	7.49	28.42
					5	0.392	0.426	0.506	8.67	29.08
					6	0.451	0.473	0.551	4.88	22.17
					7	0.415	0.397	0.425	−4.34	2.41
2	4300	900.95	105	25.994	1	0.233	0.225	0.304	−3.43	30.47
					2	0.339	0.326	0.410	−3.83	20.94
					3	0.402	0.378	0.460	−5.97	14.43
					4	0.378	0.390	0.466	3.17	23.28
					5	0.405	0.384	0.472	−5.19	16.54
					6	0.448	0.417	0.497	−6.92	10.94
					7	0.422	0.378	0.415	−7.80	1.22
3	3700	775.24	105	25.994	1	0.334	0.325	0.323	−2.69	−3.29
					2	0.363	0.357	0.440	−1.65	21.21
					3	0.426	0.408	0.489	−4.23	14.79
					4	0.419	0.414	0.495	−1.19	18.14
					5	0.411	0.420	0.501	2.19	21.90
					6	0.462	0.449	0.528	−2.81	14.29
					7	0.436	0.408	0.441	−6.42	1.15

Table 4 Process parameters for theoretical investigation

No.	Cross axis angle γ (°)	Tooth number of honing tool n_h	Rotational speed of honing tool u_h (r/min)
1	0	113	860
2	5	113	860
3	10	113	860
4	15	113	860
5	20	113	860
6	5	105	860
7	5	107	860
8	5	109	860
9	5	111	860
10	5	113	860
11	5	113	720
12	5	113	790
13	5	113	860
14	5	113	930
15	5	113	1000

The diameter of honing tool increases with tooth number n_h, which introduces the increasing rotation radius of each contact point, thereby leading to a rising $v_{wf,h}$. In Figure 6f, the curve of relative speed v changes from a V-shaped curve to an approximately straight line with an increase of angle γ. This is because that pitch radius of workpiece becomes small with the increase of angle γ, so the abscissa of the minimum relative speed becomes smaller and the corresponding contact point on workpiece tooth flank moves towards the direction of tooth root. When the point exceeds the range of active flank, a phenomenon appears that the relative speed v increases monotonically from tooth root to tooth top. In Figure 6f, the relative speeds v increase with tooth number n_h or rotational speed u_h. This is because the relative speed v is positively related to the magnitude of angular velocity $\boldsymbol{\omega}_w$, which increases with tooth number n_h and rotational speed u_h according to Eq. (1).

4.3 Effects of Process Parameters on Orientation of Machining Mark

Figure 7 shows the complete surface texture of honed gear calculated under $\gamma=5°$, $n_h=113$, and $u_h=860$ r/min. It can be clearly seen that there are numerous uniquely curved machining marks like a fish skeleton on the tooth flank. Figure 8a shows the contour map for angle λ calculated under $\gamma=5°$, $n_h=113$, and $u_h=860$ r/min. It can be observed that the angle λ first increases and then decreases gradually from tooth root to tooth top and the maximum value is 90° just located on the pitch line of workpiece. This is consistent with the change rule of machining marks orientation seen in Figure 7.

Figure 8b shows the values of calculated angle λ at $X=0$ mm under different process parameters (seen in Table 4). It can be observed that the values of angle λ are always zero when $\gamma=0°$. However, with the increasing angle γ among a range of $\gamma > 0°$, the curve of angle λ changes from a convex curve to a drop-down curve. This is because the spindles of honing tool and workpiece are parallel when $\gamma=0°$. In this case, the motion between the workpiece and the tool is equivalent to the motion of a gear pair with parallel axes. Without considering the axial displacement of workpiece, there is no velocity along the longitudinal direction for the workpiece, introducing an unchanged angle λ on the whole tooth flank of workpiece. When $0°<\gamma\leq10°$, the component of relative velocity $\boldsymbol{v}$ along the tooth profile direction has a sine function relationship with angle γ according to Eq. (3). What's more, the abscissa of the maximum relative speed becomes smaller and the corresponding contact point on workpiece tooth flank moves towards the tooth root direction, which has the same reason as that of minimal relative speed v. Thus, as shown in Figure 8b, when the angle γ is 15° or 20°, the angle λ decreases monotonically from tooth root to tooth top. If the angle γ increases to 90°, the axes of honing tool and workpiece will be perpendicular. In this case, the motion between a workpiece and a tool is equivalent to the motion of a gear pair with vertical axes. The machining marks with a longitudinal direction will be generated.

It can be seen from Figure 8b that the angle λ changes slightly with tooth number n_h at a fixed Y value. This is mainly because a small amount of change in tooth number has little effect on the change of transmission ratio i. Thus, the orientation of machining mark changes slightly according to Eqs. (23) and (24). There is no change for angle λ with honing tool rotational speed u_h at a fixed Y value. This is because the honing tool rotational speed u_h has an impact on machining efficiency, which is independent of the orientation of machining mark.

4.4 Effects of Process Parameters on Roughness

Figure 9a shows the contour map for tooth flank roughness R_a calculated under $\gamma=5°$, $n_h=113$, and $u_h=860$ r/min based on the hypothesis of spherical abrasive particles. It can be observed that the value of R_a first increases and then decreases gradually from tooth root toward tooth top. The value of R_a always remains unchanged from the left end to the right end at fixed Y value. According to Eqs. (25) and (26), the value of roughness R_a is negatively related to the ratio of $v_{wf,w}$ to $v_{wf,h}$ which is a fixed

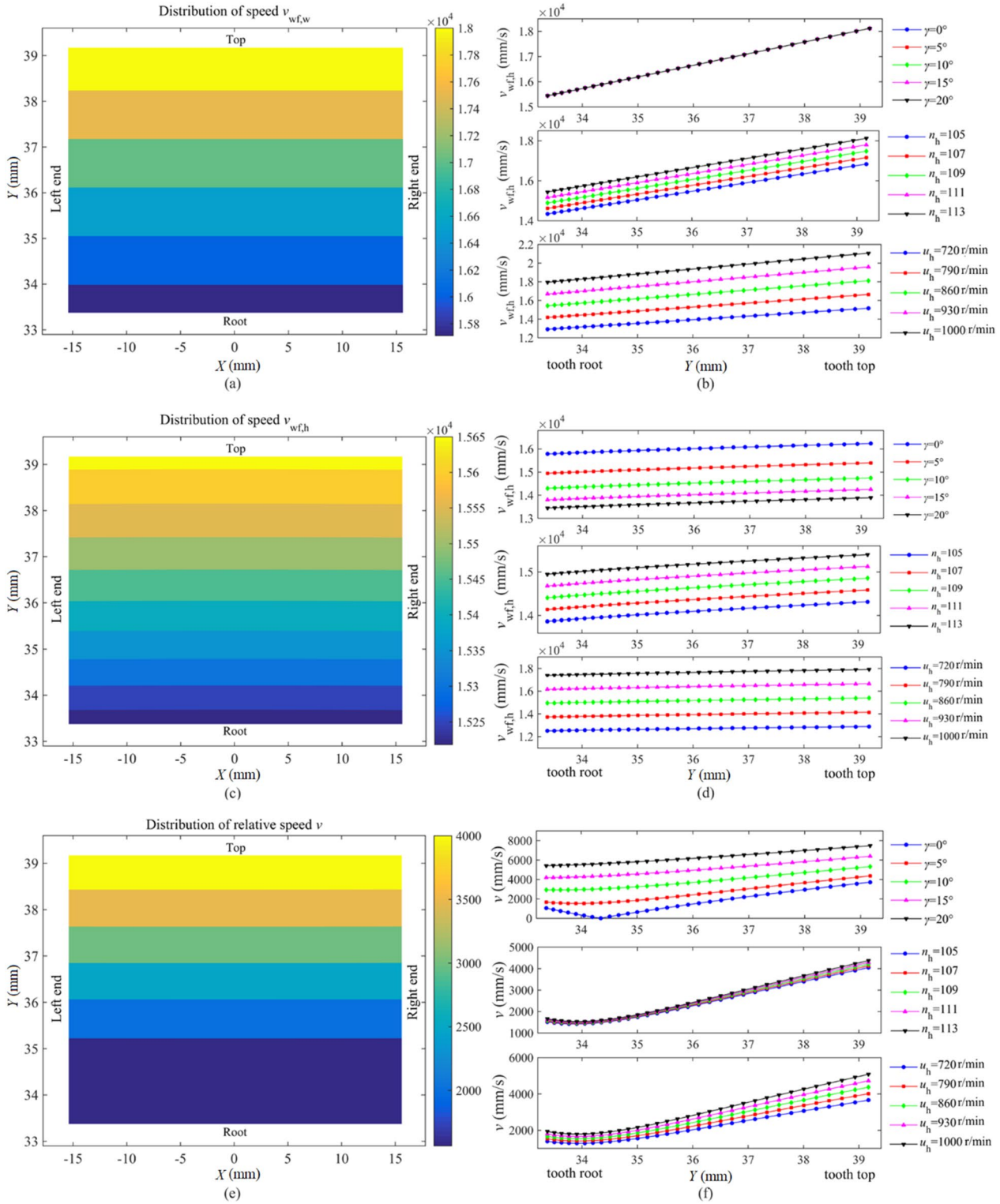

Figure 6 Contour maps for **a** speed $v_{wf,w}$ (mm/s) of workpiece along the direction of machining marks, **c** speed $v_{wf,h}$ (mm/s) of honing tool along the direction of machining mark, and **e** relative speed v (mm/s) calculated with $\gamma = 5°$, $n_h = 113$, and $u_h = 860$ r/min; **b** $v_{wf,w}$ (mm/s), **d** $v_{wf,h}$ (mm/s) and **f** v (mm/s) under different process parameters at $X = 0$ mm

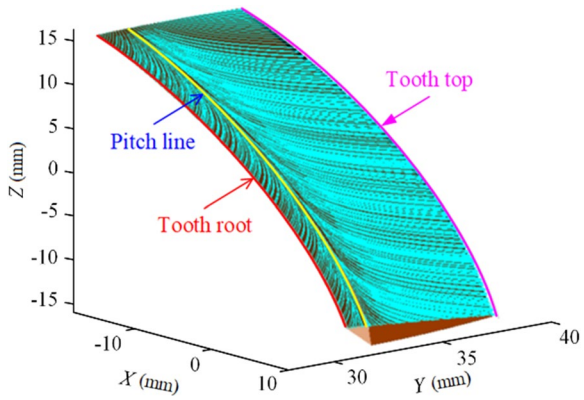

Figure 7 Calculated complete surface texture of honed gear under $\gamma = 5°$, $n_h = 113$, and $u_h = 860$ r/min

value shown in Figure 6. Besides, it is positively related to curvature $\kappa_{w,\Gamma}$ while negatively related to curvature $\kappa_{h,\Gamma}$. And the variation range of curvature $\kappa_{h,\Gamma}$ is far less than that of curvature $\kappa_{w,\Gamma}$. Therefore, the change of curvature $\kappa_{w,\Gamma}$ is a major factor for the change of roughness R_a. Figure 10 displays the calculated results for curvature $\kappa_{w,\Gamma}$ under $\gamma = 5°$, $n_h = 113$, and $u_h = 860$ r/min.

Figure 9b shows the calculated roughness R_a under different process parameters (seen in Table 4) at $X = 0$ mm. It can be observed that with the increase of angle γ, roughness R_a decreases obviously. This is mainly because the ratio of $v_{wf,w}$ to $v_{wf,h}$ increases obviously with angle γ. There are some odd large values of roughness R_a near the tooth root when $\gamma = 0°$. This is because when $\gamma = 0°$, the ratio of $v_{wf,w}$ to $v_{wf,h}$ is near 1 at the position of pitch line so Eqs. (25) and (26) are not suitable for this condition. The roughness R_a decreases slightly with the increasing tooth number n_h. This is because the transmission ratio i increases slightly with tooth number n_h, which leads to a slight increase in the ratio of $v_{wf,w}$ to $v_{wf,h}$. With the increasing honing tool rotational speed u_h, the roughness R_a decreases accordingly. This is because more abrasive particles are involved in removing workpiece material with the increasing honing rotational speed u_h. Therefore, according to Eqs. (25) and (26), the roughness R_a is reduced correspondingly, while the distribution characteristics of roughness R_a remain unchanged.

5 Conclusions

In this paper, a theoretical model of surface texture for honed gear is developed. The machining marks on tooth flank are obtained by numerical calculation. Considering the geometrical shape of abrasive particles and the plastic pile-up of gear material, a roughness model is established and then verified by experiments. The effects of process parameters on the speeds of discrete points on the tooth flank, orientations of machining marks and roughness are discussed.

The detailed conclusions are described as follows:

(1) The calculated surface texture and machining marks orientations show similar laws to the experimental results. The orientation angle of machining mark first increases and then decreases gradually from the tooth root toward tooth top, while it always remains unchanged from the left end to the

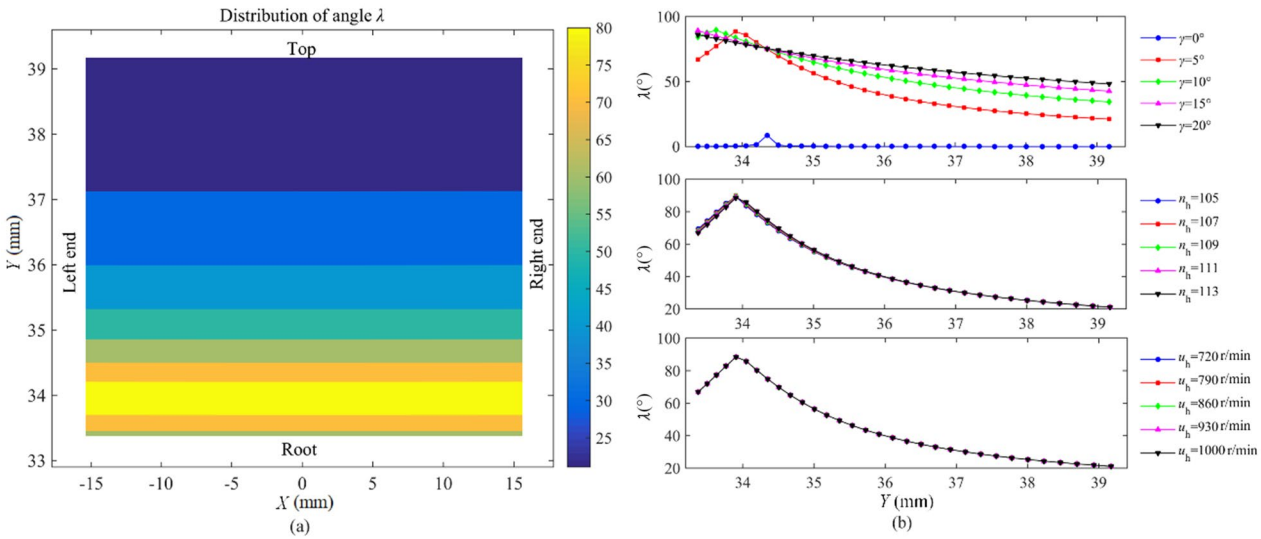

Figure 8 Calculated angle λ (degree) for machining marks: **a** the contour map under $\gamma = 5°$, $n_h = 113$, and $u_h = 860$ r/min, **b** the line chart under different process parameters at $X = 0$ mm

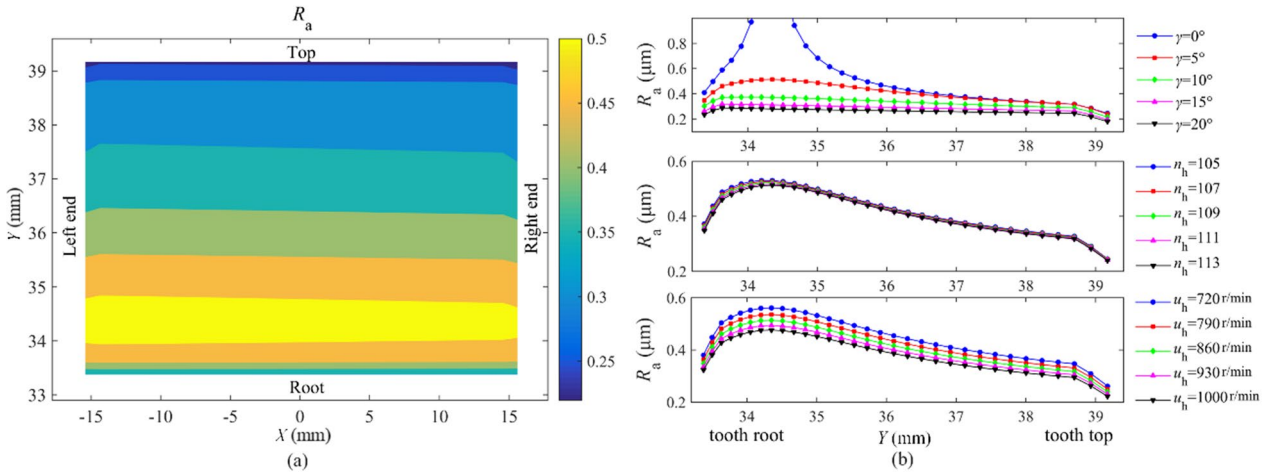

Figure 9 Calculated roughness R_a (μm) for honed gear: **a** the contour map under $\gamma=5°$, $n_h=113$, and $u_h=860$ r/min, **b** the line chart under different process parameters at $X=0$ mm

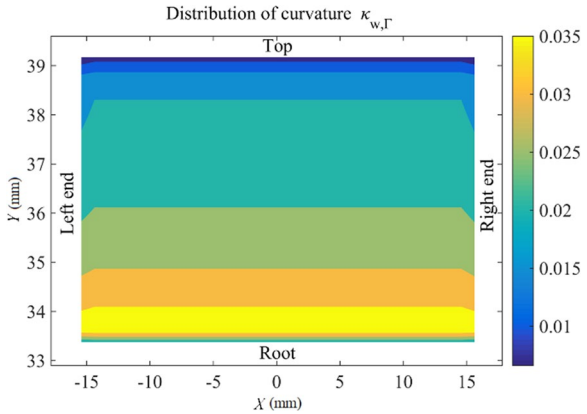

Figure 10 Curvature $\kappa_{w,\Gamma}$ (mm^{-1}) under $\gamma=5°$, $n_h=113$, and $u_h=860$ r/min

right end. The angle has a complex change with the increase of cross axis angle. Additionally, the angle changes little with the increase of tooth number, and has no change with a change of rotational speed of honing tool.

(2) The model of roughness R_a has a high calculation accuracy with a maximum error of less than 10% when the abrasive particles are assumed to be spherical. The distribution of roughness is non-uniform from tooth root to tooth top. With the increase of angle cross axis angle, the roughness decreases obviously, and the non-uniform degree of tooth flank roughness is improved effectively. The roughness decreases with the increasing tooth number or speed of honing tool.

(3) The speed of contact point along the direction of machining mark is one of main factors affecting the formation of surface texture. The relative speed first decreases and then increases gradually from the tooth root toward tooth top, while it always remains unchanged from the left end to right end. Besides, the relative speed changes from V-shaped curve to approximate straight-line with the increase of cross axis angle, and positively relates to cross axis angle and honing tool speed, respectively.

The research can provide a theoretical basis for optimization of process parameters for gear power-honing. In future, parameters optimization of honing process will be studied. The surface texture model will also be further optimized, for example by incorporating the influence of the height of the grinding grains.

Acknowledgements
Not applicable.

Author Contributions
HC and HX were in charge of the whole trial; YL wrote the manuscript; XH revised the manuscript; JW assisted with sampling and laboratory analyses. All authors read and approved the final manuscript.

Authors' Information
Yuhu Liu, born in 1997, is currently a master candidate at *State Key Laboratory of Mechanical Transmissions, Chongqing University, China.*
Xiaohui Huang, born in 1997, is currently a PhD candidate at *State Key Laboratory of Mechanical Transmissions, Chongqing University, China.*
Huajun Cao, born in 1978, is currently a professor at *Chongqing University, China.* He received his PhD degree from *Chongqing University, China*, in 2004. His research interests include advanced manufacturing technology, green manufacturing and equipment, manufacturing systems engineering.
Jiacheng Wang, born in 1995, is currently a master candidate at *State Key Laboratory of Mechanical Transmissions, Chongqing University, China.*
Huapan Xiao, born in 1988, is currently an assistant professor at *Chongqing University, China.* He received his PhD degree from *Xi'an Jiaotong University, China*, in 2020. His research interests include precision and ultra-precision abrasive processing technology and detection.

Funding
Supported by National Key Research and Development Plan (Grant No. 2020YFE0201000); Chongqing Municipal Special Postdoctoral Science Foundation (Grant No. XmT20200021); Liuzhou Municipal Science and Technology project (Grant No. 2021AAB0101).

Data availability
Data sharing is not applicable to this article as no new data were created or analyzed in this study.

Declarations

Competing Interests
The authors declare no competing financial interests.

Received: 24 June 2021 Revised: 16 June 2023 Accepted: 25 June 2023
Published online: 28 August 2023

References

[1] X Hua, A Thomas, K Shultis. Recent progress in battery electric vehicle noise, vibration, and harshness. *Science Progress*, 2021, 104(1): 1-11.
[2] P Krajnik, F Hashimoto, B Karpuschewski, et al. Grinding and fine finishing of future automotive powertrain components. *CIRP Annals-Manufacturing Technology*, 2021, 70(2): 589-610.
[3] J Han, B Yuan, D Wang, et al. Formation mechanism study on tooth surface of two gear finishing processes: combined theoretical and experimental approaches. *Journal of the Brazilian Society of Mechanical Sciences and Engineering*, 2017, 39(12): 5159-5170.
[4] D Mallipeddi, M Norell, M Sosa, et al. The effect of manufacturing method and running-in load on the surface integrity of efficiency tested ground, honed and superfinished gears. *Tribology International*, 2019 131: 277-287.
[5] D Mallipeddi, M Norell, M Sosa, et al. Effect of running-in (load and speed) on surface characteristics of honed gears. *Tribology Transactions*, 2019, 62(3): 412-418.
[6] V Rana, A Petare, N K Jain, et al. Using abrasive flow finishing process to reduce noise and vibrations of cylindrical and conical gears. *Proceedings of The Institution of Mechanical Engineers Part B-Journal of Engineering Manufacture*, 2022, 236(10): 1341-1354.
[7] A Beaucamp, B Kirsch, W L Zhu. Advances in grinding tools and abrasives. *CIRP Annals-Manufacturing Technology*, 2022, 71(2): 623-646.
[8] W Zhou, J Tang, W Shao. Study on surface generation mechanism and roughness distribution in gear profile grinding. *International Journal of Mechanical Sciences*, 2020, 187: 105921.
[9] J Han, B Yuan, L Wu, et al. Mechanism study on gear tooth surface texture in power honing process. *International Journal of Manufacturing Research*, 2017, 12: 212-224.
[10] M M Khonsari, S Ghatrehsamani, S Akbarzadeh. On the running-in nature of metallic tribo-components: A review. *Wear*, 2021, 474: 203871.
[11] M Batsch. A novel method of obtaining honing tool profile for machining gears with profile modifications. *Journal of Manufacturing Science and Engineering-Transactions of The ASME*, 2020, 142(9): 091004.
[12] V Q Tran, Y R Wu. A novel method for closed-loop topology modification of helical gears using internal-meshing gear honing. *Mechanism and Machine Theory*, 2020, 145: 103691.
[13] J Han, Y G Zhu, L Xia, et al. A novel gear flank modification methodology on internal gearing power honing gear machine. *Mechanism and Machine Theory*, 2018, 121: 669-682.
[14] T Bergs. Cutting force model for gear honing. *CIRP Annals*, 2018, 67(1): 53-56.
[15] G X Liang, M Lv, X X Gao. The relationship between the distribution characteristics of cutting speed at the contact-point and the surface quality of gear teeth. *Advanced Materials Research*, 2010, 135: 128-133.
[16] S Talu, S Kulesza, M Bramowicz, et al. Multiscale surface texture and fractal analysis of straight bevel gears finished by PECH and PECF process. *Materials and Manufacturing Processes*, 2019, 34(16): 1882-1887.
[17] B Yuan, J Han, D Wang, et al. Modeling and analysis of tooth surface roughness for internal gearing power honing gear. *Journal of the Brazilian Society of Mechanical Sciences and Engineering*, 2017, 39(9): 3607-3620.
[18] J Han, G Z Zhang. Investigation on formation mechanism of surface texture and modeling of surface roughness with internal gear power honing. *International Journal of Advanced Manufacturing Technology*, 2018, 98(1-4): 603-615.
[19] Y C Yang, Y R Wu, T M Tsai. An analytical method to control and predict grinding textures on modified gear tooth flanks in CNC generating gear grinding. *Mechanism and Machine Theory*, 2022, 177: 105023.
[20] K Matsuo, Y Suzuki, J Hongu, et al. Method of designing gear-honing-wheel geometries (Considering of relative sliding velocities). *Journal of Advanced Mechanical Design Systems And Manufacturing*, 2021, 15(1): 20-00471.
[21] K Ono, M Kawamura, M Kitano, et al. *Cutting theories*. Beijing: National Defense Industry Press, 1985. (in Chinese)
[22] T T Wang, L Zou, Q H Wan, et al. A high-precision prediction model of surface roughness in abrasive belt flexible grinding of aero-engine blade. *Journal of Manufacturing Processes*, 2021, 66: 364-75.
[23] M X Kang, L Zhang, W C Tang. Study on three-dimensional topography modeling of the grinding wheel with image processing techniques. *International Journal of Mechanical Sciences*, 2020, 167: 105241.
[24] F Elwasli, S Mzali, F Zemzemi, et al. Effects of initial surface topography and contact regimes on tribological behavior of AISI-52100/AA5083 materials' pair when reciprocating sliding. *International Journal of Mechanical Sciences*, 2018, 137: 271-283.
[25] Q Xiong, Q S Yan, J B Lu, et al. The effects of grinding process parameters of a cemented carbide micro-drill on cutting edge burr formation. *International Journal of Advanced Manufacturing Technology*, 2021, 117(9-10): 3041-3051.
[26] Q Lu, G H Zhou, F Zhao, et al. Determination of shape and distribution of abrasive grains to reduce carbon emissions of honing process. *Journal of Manufacturing Science And Engineering-Transactions of the ASME*, 2019, 141(2): 021008.
[27] T T Wang, L Zou, H Li, et al. A prediction model of residual stress for belt-grinding blade based on geometrical characteristic and progressive wear of abrasive grains. *International Journal for Numerical Methods in Engineering*, 2022, 123(12): 2814-2836.
[28] Y J Tao, G L Li, B Cao, et al. Grinding worm wear evaluation and its influence on gear surface topography in continuous generating gear grinding. *International Journal of Advanced Manufacturing Technology*, 2022, 123(9-10): 3301-3311.
[29] X Wu. *Principle of gear meshing*. Xi'an: Xi'an Jiaotong University Press, 2009. (in Chinese)
[30] X Zhou, F Xi. Modeling and predicting surface roughness of the grinding process. *International Journal of Machine Tools and Manufacture*, 2002, 42(8): 969-977.
[31] Y Liu, A Warkentin, R Bauer, et al. Investigation of different grain shapes and dressing to predict surface roughness in grinding using kinematic simulations. *Precision Engineering*, 2013, 37(3): 758-764.
[32] X Chen, W B Rowe. Analysis and simulation of the grinding process. Part II: Mechanics of grinding. *International Journal of Machine Tools and Manufacture*, 1996, 36(8): 883-896.